Published in final edited form as:
J Immunol. 2011 July 15; 187(2): 951–959. doi:10.4049/jimmunol.1003986.

IL-23 Is Critical for Induction of Arthritis, Osteoclast Formation, and Maintenance of Bone Mass

Iannis E. Adamopoulos[*,1], **Marlowe Tessmer**[*], **Cheng-Chi Chao**[*], **Sarvesh Adda**[*], **Dan Gorman**[*], **Mary Petro**[†], **Chuan-Chu Chou**[†], **Robert H. Pierce**[*], **Wei Yao**[‡], **Nancy E. Lane**[‡], **Drake Laface**[*], and **Edward P. Bowman**[*]

Iannis E. Adamopoulos: iannis.adamopoulos@ucdmc.ucdavis.edu; Edward P. Bowman: eddie.bowman@merck.com

[*]Discovery Research, Merck Research Laboratories, Palo Alto, CA 94304

[†]Department of Cardiovascular Diseases, Merck Research Laboratories, Kenilworth, NJ 07033

[‡]Center for Healthy Aging, University of California at Davis Medical Center, Sacramento, CA 95817

Abstract

The role of IL-23 in the development of arthritis and bone metabolism was studied using systemic IL-23 exposure in adult mice via hydrodynamic delivery of IL-23 minicircle DNA in vivo and in mice genetically deficient in IL-23. Systemic IL-23 exposure induced chronic arthritis, severe bone loss, and myelopoiesis in the bone marrow and spleen, which resulted in increased osteoclast differentiation and systemic bone loss. The effect of IL-23 was partly dependent on $CD4^+$ T cells, IL-17A, and TNF, but could not be reproduced by overexpression of IL-17A in vivo. A key role in the IL-23–induced arthritis was made by the expansion and activity of myeloid cells. Bone marrow macrophages derived from IL-23p19$^{-/-}$ mice showed a slower maturation into osteoclasts with reduced tartrate-resistant acid phosphatase-positive cells and dentine resorption capacity in in vitro osteoclastogenesis assays. This correlated with fewer multinucleated osteoclast-like cells and more trabecular bone volume and number in 26-wk-old male IL-23p19$^{-/-}$ mice compared with control animals. Collectively, our data suggest that systemic IL-23 exposure induces the expansion of a myeloid lineage osteoclast precursor, and targeting IL-23 pathway may combat inflammation-driven bone destruction as observed in rheumatoid arthritis and other autoimmune arthritides. *The Journal of Immunology*, 2011, 187: 951–959.

Pathological bone resorption is the result of increased differentiation and/or activity of osteoclasts (1). Osteoclast precursors differentiate into multinucleated osteoclasts in the presence of M-CSF and RANKL (2). Osteoprotegerin (OPG) is a soluble decoy receptor for RANKL that inhibits osteoclast formation and bone resorption (3). The RANK/RANKL/

Address correspondence and reprint requests to Dr. Edward P. Bowman or Dr. Iannis E. Adamopoulos, Discovery Research, Merck Research Labs, 901 California Avenue, Palo Alto, CA 94304 (E.P.B.) or Department of Internal Medicine, University of California at Davis Medical Center, Shriner's Hospitals for Children Northern California, 2425 Stockton Boulevard, Research, 6th Floor, Room 650, Sacramento, CA 95817 (I.E.A.).

[1]Current address: Department of Internal Medicine, University of California at Davis Medical Center, Shriner's Hospitals for Children Northern California, Sacramento, CA.

I.E.A. is the recipient of an Arthritis National Research Foundation fellowship.

The online version of this article contains supplemental material.

Disclosures

I.E.A., M.T., C.-C. Chao, S.A., D.G., M.P., C.-C. Chou, R.H.P., D.L., and E.P.B. were employees of Schering-Plough at the time of these studies. Schering-Plough Biopharma (formerly DNAX Research, Inc.) is now part of Merck Research Laboratories. The other authors have no conflicts of interest.

OPG axis governs homeostatic bone remodeling, as mice deficient in RANK, RANKL, or OPG have severe bone phenotypes (2–4).

Activated $CD4^+$ T cells also produce RANKL and other pro-inflammatory factors, such as TNF, which stimulate osteoclastogenesis in $RANK^{-/-}$ mice (4), demonstrating that inflammation-mediated osteoclastogenesis can lead to joint pathology (5–7). IL-23 is a proinflammatory cytokine composed of the IL-23p19 and IL-12/23p40 subunits. IL-23 promotes the differentiation of a novel CD4 memory T cell subset (Th17), which is distinct from the classical Th1 and Th2 memory T cell subset. Th17 cells are characterized by their production of the signature cytokine IL-17A. IL-17A contributes to arthritis progression and promotes the production of RANKL by osteoblasts, synoviocytes, and up-regulating RANK on osteoclast precursors (8–11). IL-17R-dependent signals are essential in preventing pathogen-initiated bone destruction through neutrophil recruitment (12, 13). More recently, a bone-protective role for IL-17R was described in ovariectomy-induced bone loss through negative regulation of adipogenesis and leptin expression (14). These data emphasize the complex role of IL-17A signaling in bone loss.

Murphy et al. (15) demonstrated that IL-$23p19^{-/-}$ mice did not experience development of collagen-induced arthritis and were therefore unable to develop inflammation-driven autoimmune joint destruction. Similarly, Sato et al. (10) observed that LPS-driven osteoclast formation in vivo was reduced in the absence of IL-23 (16). It was recently reported that IL-23 stimulates the formation of functional osteoclasts in human PBMC cultures and the expression of RANK in mouse osteoclast progenitor cells (17, 18), suggesting that IL-23 has pro-osteoclastogenic properties. Other groups using in vitro cell culture systems have reported that IL-23 has an indirect inhibitory effect on osteoclast formation involving GM-CSF (19).

In this article, we examined the bone and joint pathology of adult mice overexpressing IL-23 using hydrodynamic delivery of IL-23 minicircle (MC) DNA, and further evaluated osteoclast formation and bone mass in IL-$23p19^{-/-}$ mice. Collectively, the data support that IL-23 can be a potent inducer of bone erosion independent of IL-17A–producing $CD4^+$ Th17 cells. Moreover, IL-23 is implicated in the development of mature osteoclasts and the maintenance of bone mass in adult mice.

Materials and Methods

Reagents and Abs

All cell incubations were performed in culture medium consisting of αMEM (Invitrogen, Carlsbad, CA), 2 mM glutamine, 10% heat-inactivated FBS (Invitrogen), 100 IU/ml penicillin, and 100 μg/ml streptomycin. Mouse soluble RANKL (sRANKL), OPG, TNF, and OPG ELISA were from R&D Systems (Minneapolis, MN). Mouse RANKL ELISA was performed using an in-house mouse monoclonal RANKL Ab previously described (19). Clodronate and unloaded liposomes were from Encapsula Nano Science (Nashville, TN). The depleting rat anti-CD4 (GK1.5) and the Luminex for MIP-3α, TNF, GM-CSF, IFN-γ, IL-4, IL-6, IL-10, IL-17A, IL-17F, IL-25, IL-21, IL-22, and IL-27 was obtained from BioLegend (San Diego, CA). The neutralizing rat anti-mouse IL-17A Ab (1D10) was developed at Schering Plough Biopharma/DNAX Research, Inc., as previously described (20). Abs were dosed 72 h before gene transfer and at 72-h intervals for 11 d at a concentration of 25 mg/kg. Clodronate was dosed at 5 mg/kg. Depletion was evaluated as described under flow cytometry methods.

A fusion protein consisting of mouse TNFR2 (mTNFR2) bound to the Fc portion of mouse IgG1 (mIgG1) was used to neutralize TNF. The mTNFR2-mIg protein was designed by

fusing the extracellular domain of mTNFR2 (GenBank accession number NP_035740: http://www.ncbi.nlm.nih.gov/protein/NP_035740) at its C terminus to a partial mIgG1 H chain (GenBank accession number AAB06744: http://www.ncbi.nlm.nih.gov/protein/AAB06744) starting with the hinge region and spanning the entire CH2 and CH3 regions. A linker of glycine-serine dipeptide was introduced for the convenience of assembly of the cDNA via BamH1 restriction digestion followed by ligation. In brief, the cDNA of the mTNFR2 extra-cellular region was cloned by reverse transcription PCR from a mixture of RNA isolated from mouse spleen, mouse liver, and mouse macrophage-like RAW264.7 cells using oligonucleotide primers 5′-GATGAATTC-GCCGCCACCATGGCGCCCGCCGCCCTCTGGGTC-3′ and 5′-GATG-GATCCGCCACCCTTGGTACTTTGTTCAATAATGGG-3′. The resulting cDNA was cleaved using EcoR1 and BamH1 endonucleases and cloned into a pCDNA3-based vector containing a DNA corresponding to mIgG H chain γ1 isotype starting at the hinge region and ending at the CH3 region. mTNFRII-mIgG1 was transfected into CHO-K1 variant of Chinese hamster ovary cells by Lipofectamine 2000 according to manufacturer's instructions (Invitrogen). Stable clones were obtained by limiting dilution followed by culturing in the presence of selection reagent Geneticin at 1 mg/ml. High-producer clones were identified by testing the conditioned medium with ELISA using an mIgG1 ELISA kit (Bethyl Laboratories, Montgomery, TX). For production of the mTNFRII-mIg protein, the cells were cultured under serum-free conditions for 7 d. The conditioned medium after centrifugation was passed through a protein A-affinity column and purified using the Bio-Rad purification system (Hercules, CA).

In vitro mouse TNF-α neutralization bioassay

HEK293 cells stably transfected with a NF-κB–responsive element-luciferase reporter gene were prepared and maintained in DMEM high glucose supplemented with 10% heat-inactivated FBS, penicillin-streptomycin, 4 mM L-glutamine, 10 mM HEPES, and 1 mg/ml Geneticin (Invitrogen, Carlsbad, CA) in a 5% CO_2 atmosphere at 37°C. Cells were seeded into white 96-well culture plates at 1×10^6 viable cells/ml in 50 μl volume of medium listed earlier and allowed to adhere overnight in a 5% CO_2 atmosphere at 37°C. On the day of assay, mTNFRII-mIg and mouse TNF-α (R&D Systems) were each prepared and diluted in DMEM containing 0.1% BSA. The two reagents were mixed at indicated concentrations and preincubated for 30 min at 37°C. The mixtures were then added in 10-μl volumes to cells in the wells and the incubation was continued for 4 h, after which steadylite HTS (Perkin Elmer, Waltham, MA) was added to the wells at 60 μl/well, and plates were agitated for 10 min followed by reading on an Envision Luminometer (Perkin Elmer). The EC_{50} values were calculated using the PRISM program (GraphPad Software, La Jolla, CA).

Mice and mouse osteoclast cultures

All animal protocols were approved by Schering-Plough Biopharma's Institutional Animal Care and Use Committee. Control wild-type C57Bl6 mice were purchased from Jackson Laboratories (Sacramento, CA). B6.129–IL-23p19^{tm1DNAX} (IL-23p19$^{-/-}$) mice have been previously described (21). Mice were sacrificed by carbon dioxide exposure and serum prepared from cardiac puncture collected blood. Whole bone marrow was extracted from tibia and femurs of 8-wk-old control C57BL/6 and IL-23p19$^{-/-}$ mice. Cells were plated in culture medium containing 25 ng/ml M-CSF for 4 d. Osteoclasts were generated in subsequent 5-d cultures of bone marrow macrophages (BMM) with 25 ng/ml M-CSF and 50 ng/ml sRANKL.

Production and purification of IL-23 and IL-17A minicircle DNA

The original minicircle producing vector obtained from Mark Kay (Stanford University) was re-engineered by introducing unique PmeI and PacI restriction sites downstream of attB sites

of the original plasmid. The sequence encoding a Flag-tagged linked mouse IL-23 (mIL-23-elastikine) or mouse IL-17A was inserted under the control of Rous Sarcoma virus (RSV) promoter in the unique PmeI and PacI restriction sites (Supplemental Fig. 1). Minicircle-RSV.Flag.mIL23.elasti.bpA or minicircle-RSV.mIL17A. elasti.bpA was produced as described by Chen et al. (23) with minor modification to prepare a 1-l culture. A single isolated colony from a fresh plate was grown for 8 h in 2 ml Luria-Bertani broth with ampicillin. Eight hundred microliters of this culture was used to inoculate 1 l Terrific broth and grown for an additional 17 h. Overnight cultures were centrifuged at 20°C, 4000 rpm for 20 min. The pellet was resuspended 4:1 (v/v) in fresh Luria-Bertani broth containing 1% L-arabinose. The bacteria were incubated at 32°C with constant shaking at 250 rpm for 2 h. After adding half volume of fresh low-salt Luria-Bertani broth (pH 8.0) containing 1% L-arabinose, the incubation temperature was increased to 37°C and the incubation continued for an additional 2 h. Episomal DNA circles were prepared from bacteria using plasmid purification kits from Endofree Qiagen Megaprep (Chatsworth, CA). Minicircle DNA was dialyzed against 1× Tris-EDTA buffer overnight at 4°C.

IL-23 minicircle-induced arthritis model

Hydrodynamic delivery involves rapid delivery of naked DNA in a relatively large volume of physiological solution using the tail vein. DNA is delivered to mice in a total volume of ~10% of the mice body weight within a period of 5–7 s. These seemingly harsh conditions actually cause little harm and are well tolerated (22). MC DNA vectors devoid of bacterial DNA, when delivered via hydrodynamic procedure, can result in persistent and high-level transgene expression in vivo (23). In this study, we combined hydrodynamic method of gene delivery and MC DNA to achieve a high and sustained level of IL-23 gene expression in vivo.

Histological analysis of inflamed joints

Paws and knees were fixed in 10% neutral buffered formalin, decalcified in EDTA solution, embedded in paraffin, and stained. Sections were scored by board-certified pathologist who were blinded to treatment groups and analyzed by a categorical scoring system as previously described (24).

Specimen preparation and image acquisition by microcomputer tomography

Hind paws and knee were amputated from control and IL-23 MC-injected mice at 8 wk postinjection and at the age of 15 wk. The specimens were fixed in cold 10% neutral buffered formalin for 2 d and were washed with running water for 15 min just before scanning. Microcomputer tomography (μCT) was performed with GE eXplore Lotus μCT scanner (GE Healthcare, Piscataway, NJ) on excised paws and knees. Data were acquired at 27-μm isotropic voxel size with 720 projections by 360-degree scan, integration time of 2000 ms with three frames, photon energy of 80 KeV, and current of 450 μA. Three-dimensional image rendering was generated through original volumetric reconstructed images using Microview software (GE Healthcare).

High-resolution μCT scans of mouse femurs and tibias were scanned at Numira Biosciences (Salt Lake City, UT) using a high-resolution volumetric μCT40 scanner (Scanco Medical AG, Bassersdorf, Switzerland). The image data were acquired at 6-μm isometric voxel resolution at 300 ms exposure time, 2000 views, and 5 frames/view. The μCT-generated DICOM files were used to analyze the samples and to create volume renderings of the region of interest. Using Scanco Medical software, we obtained bone density measurements for the femur's midshaft and distal end. For distal femur analysis, a three-dimensional trabecular volume (TV) was selected 0.5 mm below the growth plate and 0.5 mm thick. For midshaft analysis, the length of the entire femur was measured, and a 1-mm-thick

midcortical section was used for analysis. A threshold of 20% of the 16-bit total grayscale values between 0 and 32,000 was used.

Bone histomorphometry

After fixation in 10% formalin, the right femurs were dehydrated in graded concentrations of ethanol and xylene, and embedded undecalcified in methyl methacrylate. The frontal sections (4 μm thick) were cut using a vertical bed microtome (Leica/Jung 2265) and affixed to slides coated with a 2% gelatin solution. The sections were stained with von Kossa and counterstained with toluidine blue. Bone histomorphometry was performed using a semiautomatic image analysis (Bioquant Image Analysis Corporation, Nashville, TN) linked to a microscope equipped with transmitted and fluorescent light. The analyses were performed in the secondary spongiosa of the distal femurs that included trabecular area between 50 and 200 μm distal to the growth plate and excluding the cortex. Trabecular bone area, perimeter, osteoclast number (OcN), and osteoclast surface (OcS) were measured. These indices were used to calculate trabecular bone volume (BV/TV), percentage of OcS, and osteoclast/OcS (25).

Cytochemical and functional assessment of osteoclast formation

The cells cultured on plastic dishes were stained for tartrate-resistant acid phosphatase (TRAP) using a commercial kit (387-A; Sigma) according to manufacturer's instructions. Dentine slices were fixed with 4% formaldehyde for 5 min and then permeabilized for 6 min in 0.5% Triton X-100 (in PBS) and rinsed with PBS to detect F-actin ring structure. The cells on dentine slices were then incubated with 0.1 μM tetramethylrhodamine isothiocyanate-conjugated phalloidin (Sigma-Aldrich) for 30 min, washed and rinsed with PBS before mounted with DAPI (Vectashield; Vector Laboratories), and observed using a fluorescence microscope (Nikon). Functional evidence of osteoclast formation was determined by a lacunar resorption assay system using cell cultures on dentine slices as previously described (11). Cells on dentine were fixed in 4% glutaraldehyde, dehydrated by passing through graded alcohols, and then through graded (50–100%) hexamethyldisilazane solution (Sigma-Aldrich, St. Louis, MO) before being air-dried. Dentine slices were then mounted onto aluminum stubs (EMS), sputtered with gold, and examined using a Philips SEM 505 scanning electron microscope.

RNA extraction and real-time quantitative PCR

Total RNA was purified from different stages of osteoclast cultures using the RNAeasy Mini Kit (Qiagen). Gene expression was calculated using the Δ−ΔCt method (using the mean cycle threshold [Ct] value for ubiquitin and the gene of interest for each sample). The equation $1.8e(\text{Ct ubiquitin} - \text{Ct gene of interest}) \times 10^4$ was used to obtain the normalized values.

Flow cytometry of isolated BMM and lymphocytes

Bone marrow cells were flushed from femurs and tibia of C57BL/6 and IL-23p19$^{-/-}$ mice and dispersed to single-cell suspensions. Nonspecific binding was blocked by pretreating cells with rat anti-mouse CD16/32 mAb (clone 2.4G2) 10 min at room temperature. Alexa Fluor 647-conjugated rat anti-mouse CD11b mAb (M17), PE-conjugated rat anti-mouse Gr-1 mAb (RB6-8C5), and isotype controls were all obtained from BD Biosciences (San Jose, CA). CD11b PE-Cy7 and GR-1 Pacific blue were purchased from eBioscience (San Diego, CA). Cells were incubated with 2.4G2 anti-CD16/32 receptor mAb and stained with indicated Abs. Spleens were minced and passed through a 70-μm nylon cell strainer (BD Falcon, Bedford, MA), and bone marrow cells were flushed from femurs of B10.RIII mice. Cell suspensions were layered on Lympholyte-M (Cedar-lane Laboratories), centrifuged for

20 min at 900 × *g*, collected and washed once in 2% serum in PBS. Events were collected on a FACSCalibur or LSR II flow cytometer (BD Biosciences) and analyzed using FlowJo software (Tree Star, Ashland, OR).

Statistical analysis

Data were analyzed using Mann–Whitney *U* test. One-way or two-way ANOVA with Bonferroni after test were used where appropriate. A p value <0.05 was considered to be statistically significant (minimum $n = 3$).

Results

Hydrodynamic delivery of IL-23 MC induces immune-mediated joint-destructive arthritis and bone loss in vivo

IL-23 transgenic mice die early from multiorgan inflammation, which limits their use in studying the osteoclastogenesis potential of IL-23 (26); therefore, IL-23 was overexpressed in adult mice using minicircle DNA (IL-23 MC) administered by hydrodynamic delivery to probe the effect of IL-23 on osteoclast development and function. A minicircle cDNA (3 μg/ml) construct encoding IL-23p19 and IL-12/23p40 linked together or GFP control was injected i.v. into male B10RIII mice. Quantitation of serum IL-23 taken from periodic tail bleeds demonstrated that IL-23 was stably expressed for a period of at least 90 d and caused chronic paw swelling response. Examination of H&E-stained decalcified limb samples from the IL-23 MC-injected mice at 30 d after gene transfer (Fig. 1*A*) demonstrated a constellation of histopathologic findings including severe bone marrow hyperplasia with a prominent myeloid shift in association with extensive loss of sub-chondral epiphyseal bone and metaphyseal trabecular bone. Extensive erosion of cortical bone was also noted. The synovium was hyperplastic and inflamed, containing a mixed inflammatory in-filtrate consisting of mononuclear cells and numerous polymorphonuclear leukocytes. Neovascularization and proliferation of fibrocellular pannus was pronounced. In some areas, the pannus had eroded into adjacent cartilage and, occasionally, completely obliterated the normal joint architecture. Immunohistochemistry confirmed the presence of neovascularization ($CD31^+$ vascular structures), as well as the involvement of $F4/80^+$, $CD3^+$, and $B220^+$ cells within the infiltrate (data not shown). Taken together, these histopathologic features are consistent with an immune-mediated joint-destructive arthritis.

IL-23–mediated structural damage to the skeleton was easily demonstrated using μCT analysis. Severe bone damage in IL-23 MC–injected mice occurred in the phalangeal (metatarsal, proximal, distal) joints and in all subsets of the paw tarsal bones. The paw swelling response was severe, occurred in both the front and back paws, and was highly reproducible in all IL-23 MC mice (Fig. 1*B*), but never observed in GFP MC mice. Severe bone damage also occurred in the distal end of femur and proximal end of tibia of the knee (Fig. 1*C*). The bone damage was not limited to just articular joints, as significant systemic decreased bone mineral density was observed (Fig. 1*D*). Increased serum levels of TNF, IL-6, IL-17A, IL-17F, IL-21, IL-22, IFN-γ, and GM-CSF were noted in late-stage arthritic mice, 28 d after IL-23 MC injection (Fig. 1*E*).

Systemic IL-23 induces myelopoiesis, serum TRAP5b, and IL-17A

The prominent myeloid shift observed in the bone marrow by histology correlated with an increase in the myeloid $CD11b^+$ population in the bone marrow and spleen as assessed by flow cytometry (Fig. 2*A*, 2*B*). Similarly, the prominent bone resorption seen by μCT correlated with an elevation in the osteoclast-associated marker TRAP-5b in the serum (Fig. 2*C*). Serum from early arthritic mice (day 11) was analyzed for changes in levels of cytokines and chemokines to investigate the arthritis initiation mechanism. Systemic serum

IL-23 levels driven by the IL-23 MC gene transfer were detected (Fig. 2*D*), as well as statistically significant increases in the IL-23 signature cytokines IL-17A (Fig. 2*D*), IL-17F (71 ± 45 versus 16 ± 1 pg/ml), and IL-22 (510 ± 287 versus 44 ± 21 pg/ml). Day 11 serum levels of sRANKL, GM-CSF, IFN-γ, IL-4, IL-6, and IL-21 were not consistently significantly different from control mice (data not shown, $n = 3$ independent experiments); notably, serum TNF levels were not significantly increased at day 11 (Fig. 2*D*). We further focused on the known osteoclastogenic factors IL-17A and TNF in this report to evaluate the mechanism by which chronic IL-23 exposure can drive profound bone loss. The two other IL-23 signature cytokines IL-17F and IL-22 that were elevated at early time points coincident with elevated TRAP5b do not have a known inhibitory or pro-osteoclastogenic action.

Systemic IL-17A did not induce arthritis, and depletion of IL-17A–producing CD4 T cells in the IL-23 gene transfer model provided some protection from arthritis and bone loss

IL-17A MC DNA was injected in vivo to establish stable chronic expression of IL-17A to evaluate the role of IL-17A in arthritis initiation. IL-17A was robustly upregulated by day 11 after IL-23 MC injection; however, no sign of paw inflammation was observed after 8 wk of IL-17A exposure, suggesting that IL-17A was incapable of arthritis initiation (Fig. 3*A*). IL-23 induces TNF expression, and TNF transgenic mice experience development of chronic arthritis that leads to joint destruction (26, 27). TNF blockade had a small inhibitory effect on the clinical score of the disease, but was not adequate to prevent IL-23–mediated arthritis (Fig. 3*A*), and also had a moderate effect on IL-23 elevated serum TRAP5b (Fig. 3*B*).

To identify whether the cellular and molecular mechanisms for IL-23–induced arthritis required IL-17A, TNF, or $CD4^+$ T cells, we depleted $CD4^+$ T cells and neutralized IL-17A and TNF. Blocking IL-17A or TNF and depletion of $CD4^+$ cells provided some protection against arthritis development, as well as modulating osteoclast biomarker serum TRAP5b. These data suggested that IL-23 MC-arthritis induction and osteoclast formation is only partly dependent on IL-17A, TNF action, and IL-17A–producing $CD4^+$ T cells (Fig. 3).

Next, we investigated whether the myeloid shift observed in the IL-23 MC-injected mice was directly related to arthritis initiation. Depletion of phagocytic cells showed a marked decrease in arthritis induction (Fig. 3*A*) and serum TRAP5b (Fig. 3*B*).

IL-23p19$^{-/-}$ mice develop osteoclasts that have impaired differentiation and function

Because osteoclast precursors are within the population of phagocytic cells and IL-23 affects the myeloid population, the impact of IL-23 deficiency during in vitro osteoclastogenesis cultures was investigated to distinguish whether IL-23 directly affects osteoclastogenesis. BMM isolated from wild-type and IL-23p19$^{-/-}$ mice had equal numbers of $CD11b^+$ cells (osteoclast precursors; Fig. 4*A*), and when stimulated with M-CSF and RANKL, these osteoclast precursors differentiated into multinucleated $TRAP^+$ cells (Fig. 4*B*) capable of F-actin ring formation (data not shown) and dentine resorption (Fig. 4*C*). However, differences were observed in the osteoclast differentiation cultures and in the activity of the mature osteoclasts in the absence of IL-23p19. Quantitative gene expression analysis showed that the osteoclast-related gene TRAP5b was not upregulated to the same extent in in vitro BMM differentiation cultures from IL-23p19$^{-/-}$ mice compared with control mice at day 4, although TRAP5b message levels were at similar levels by day 8. No other osteoclast-related genes were significantly different by gene expression at these time points (data not shown). In agreement with gene expression data, cytochemical TRAP staining at day 6 was significantly reduced in IL-23p19$^{-/-}$ BMM cultures compared with control wild-type BMM cultures (Fig. 4*B*). Finally, functional assays showed that BMM isolated from IL-23p19$^{-/-}$

had reduced osteoclast activity and resorbing capacity compared with control mice (Fig. 4*C*).

Twenty-six-wk-old male IL-23–deficient mice have bone abnormalities caused by osteoclast dysregulation

Unmanipulated 8-wk-old IL-23p19$^{-/-}$ mice were examined to investigate whether homeostatic levels of IL-23 in vivo had any effect in physiological bone remodeling. The bone mineral density of the cortical and trabecular bone was not significantly different between control and IL-23p19$^{-/-}$ male mice (Supplemental Fig. 2*A*, 2*B*). Serum RANKL and OPG levels in IL-23p19$^{-/-}$ mice were similar to control mice (Supplemental Fig. 2*C*), suggesting that IL-23 does not play a significantly discernible role in physiological bone remodeling of young adult mice.

We studied unmanipulated 26-wk-old IL-23p19$^{-/-}$ mice to investigate whether basal IL-23 played any role in older mice and/or whether IL-23 deficiency would cause a progressive bone phenotype that was not discernible in young adult mice. Compared with the control mice, IL-23p19$^{-/-}$ mice had a trend to higher cancellous bone volume (BV/TV), ~30% more trabecular numbers (Tb.N), and the trabecular separation was decreased by 28% ($p < 0.05$) at the distal tibial metaphysis (Fig. 5*A*–*C*). The OcS/BS was decreased by 47% in IL-23p19$^{-/-}$ mice compared with the control group ($p < 0.05$; Fig. 5*D*). Interestingly, the number of OcN/BS was inversely proportionally increased in IL-23p19$^{-/-}$ mice compared with the control group.

Discussion

IL-23 is a proinflammatory cytokine implicated in rheumatoid arthritis, psoriasis, ankylosing spondylitis, autoimmune inflammation of the brain, and inflammatory bowel disease (21, 28, 29). IL-23 was overexpressed in adult mice using hydrodynamic delivery of IL-23–encoding MC DNA to elucidate the actions of IL-23 in vivo. This nonviral gene transfer model allows IL-23 protein to be stably expressed by hepatocytes (30), creating stable IL-23 serum levels over 15 wk. Systemic IL-23 expression led to hyperplastic and inflamed synovium containing a mixed inflammatory infiltrate consisting of mononuclear cells and numerous polymorphonuclear leukocytes. The paw inflammation was severe and highly reproducible in all IL-23 MC-injected mice. The pronounced proliferative and fibrocellular pannus eroded into adjacent cartilage and, occasionally, completely obliterated the normal joint architecture. Systemic IL-23–mediated structural damage to the skeleton was easily demonstrated using μCT analysis. Profound bone loss is common in autoimmune arthritis models at sites proximal to the inflammation. There are at least three types of pathological bone loss: focal articular, periarticular, and systemic. All three types of bone loss were observed by IL-23 overexpression, and the systemic bone loss was more severe than in any experimental arthritis model that we have used preclinically.

It was anticipated that the IL-23–dependent bone pathology would be dependent on IL-17A because IL-23 regulates (in conjunction with IL-6 and TGF-β) the differentiation of naive T cells into CD4$^+$ Th17 cells that secrete IL-17A (31), and IL-17A was one of the first cytokines to be detected in the serum after IL-23 MC injection. Depletion of CD4$^+$ T cells before IL-23 MC injection modestly reduced the clinical score but did not fully inhibit arthritis initiation, suggesting that IL-23 MC arthritis induction did not require CD4$^+$ T cells. Because IL-17A can be produced by cell types other than CD4$^+$ Th17 cells, we neutralized IL-17A before IL-23 MC injection. Although IL-17A neutralization slowed the progression of paw inflammation, it did not inhibit disease onset. The moderate effect of depleting CD4$^+$ T cells and IL-17A neutralization suggest that IL-23 MC arthritis initiation and bone loss in this model did not require Th17 cell differentiation. Furthermore, chronic expression of

IL-17A did not induce arthritis or paw swelling, suggesting that the actions of IL-23 are independent of IL-17A.

Depletion of phagocytic cells markedly decreased the IL-23 MC-mediated arthritis score and almost completely alleviated paw swelling. Macrophages and dendritic cells are the only known phagocytic cells that can differentiate to osteoclasts (32), and macrophages can differentiate into osteoclast-like cells via IL-17A, as well as TNF (9). Although TNF transgenic mice experience development of arthritis and IL-23 induces TNF expression (26, 27), neutralization of TNF had a modest inhibitory effect on the clinical score of the disease but was not sufficient to prevent arthritis induction.

The osteoclast precursor has not yet been identified based on a unique profile of flow cytometry markers, but osteoclasts have been generated from precursors found in many cell subsets including $CD11b^+$ and $CD11c^+$ cells (33, 34). Flow cytometry data showed that clodronate treatment reduced IL-23 elevated serum TRAP5b, but also reduced $CD11c^+$ cells to a greater extent than $CD11b^+$ cells (data not shown). This suggests that IL-23 may induce the differentiation of immature dendritic cells into osteoclasts. Moreover IL-23 stimulated osteoclast formation from human PBMCs but failed to induce osteoclast formation from the purified $CD14^+$ fraction in vitro (17). Therefore, it is unclear whether IL-23–induced myelopoiesis affects more than one myeloid subtype, and hence more than one type of osteoclast precursors.

The link between phagocytic cells and the dramatic bone loss phenotype led us to study the direct effect of IL-23 on the differentiation of osteoclast precursors into bone-resorbing osteoclasts. An in vitro culture system using BMM from IL-23p19$^{-/-}$ mice cultured in the presence of M-CSF and RANKL was used to examine this question. Functional and cytochemical assays showed a marked decrease in TRAP message at day 4 that correlated with reduced $TRAP^+$ cells present in day 6 BMM cultures. The delay in osteoclast maturation can be partly explained by the recent demonstration that IL-23 upregulates RANK expression in mouse BMM and promotes commitment of myeloid precursor cells to RANKL-mediated osteoclastic differentiation (18). It was noteworthy that the actions of IL-23–induced RANK induction were IL-17A independent.

The in vivo significance of the in vitro delay in osteoclast maturation was studied using unmanipulated IL-23–deficient mice and evaluating their bone mass and bone structure. The cortical and trabecular bone mineral density of control and IL-23–deficient 8-wk-old male mice was not statistically different using 6-μm high-resolution μCT analysis. These data were in agreement with a previous study using 40-μm resolution dual-energy X-ray absorptiometry that revealed no obvious abnormality in skeletal development and bone morphometric analyses, and concluded that bone resorption and formation was normal in IL-23p19$^{-/-}$ mice (10). In our studies, there was no detectable modulation of physiologic bone remodeling in mice deficient in IL-23 biology, and serum RANKL and OPG levels were similar to control mice (Supplementary Fig. 2). These findings suggest that compensatory mechanisms in vivo could correct for delayed macrophage to osteoclast differentiation.

Interestingly, compared with the control mice, 26-wk-old IL-23p19$^{-/-}$ mice showed a higher trend in cancellous bone volume (BV/TV), which was not statistically significant, ~30% more Tb. N, and the trabecular separation was decreased by 28% ($p < 0.05$) at the distal tibial metaphysis (Fig. 5). The OcS/BS was also decreased by 47% in IL-23p19$^{-/-}$ mice compared with the control group ($p < 0.05$; Fig. 5*D*). Interestingly, the number of OcN/BS was inversely proportionally increased in IL-23p19$^{-/-}$ mice compared with the control group.

In this study, we did not observe a progressive osteopenia as previously suggested (19). Using 6-μm high-resolution μCT analysis to measure bone mass, we deduced that the trabecular thickness is ~30 μm at 8 wk of age and increases to ~40 μm at 26 wk of age in male mice. Quinn et al. (19) used 70-μm resolution peripheral quantitative CT, which we suspect might not be able to detect small-size mouse trabeculae and underestimated the bone mass. Alternative explanations for the discrepancies between our findings and those of Quinn et al. could be the use of different IL-23–deficient mouse strains and/or the extent to which the IL-23–deficient mice used by Quinn et al. were backcrossed to the C57BL/6 background.

Nonetheless, histomorphometry analysis revealed an increase in the OcN in IL-23p19$^{-/-}$ mice compared with the control group, and these data are in agreement with Quinn et al.'s study (19). However, because these osteoclasts are of much smaller size (47%) compared with control group, we believe that these are immature osteoclasts, which are poorly fused and exhibit a much slower differentiation capacity than the control group, as the decreased in vitro osteoclastogenesis potential of BMM from IL-23p19$^{-/-}$ mice also showed. Therefore, our interpretation is that the increased number of osteoclasts with a decreased ratio of OcS to trabecular BS present in the IL-23–deficient mouse is due to an inhibition of the fusion process of osteoclast differentiation. Our data are also in agreement with other independent observations that support the general notion of IL-23 as a pro-osteoclastogenic rather than anti-osteoclastogenic cytokine (17, 18). These results indicate that IL-23 plays a significant role in the expansion, maturation, and differentiation of myeloid lineage osteoclast precursor, and the regulation of this cell by IL-23 affects the maintenance of bone mass in adult mice.

In summary, systemic IL-23 exposure drives a severe arthritis that causes a profound bone-resorptive phenotype. Depletion and neutralization strategies to uncover the mechanisms of bone destruction in this model suggest that IL-23 induces osteoclastogenesis and bone loss through the "traditional" osteoclastogenic IL-17A–producing CD4^{+} Th17 cell, as well as through the induction of a myeloid lineage osteoclast precursor. Our data suggest that IL-23 is a suitable target to combat inflammation-driven bone destruction, as observed in rheumatoid arthritis and other autoimmune arthritides.

Supplementary Material

Refer to Web version on PubMed Central for supplementary material.

Acknowledgments

We thank Carol Terminelli for technical assistance on the production of mTNFRII-Ig and Rene De wall Malefyt for critical reading of the manuscript.

This work was supported by Schering-Plough/Merck Corporation.

Abbreviations used in this article

BMM	bone marrow macrophages
BS	bone surface
BV/TV	trabecular bone volume
Ct	cycle threshold
μCT	microcomputer tomography

MC	minicircle
mIgG1	mouse IgG1
mTNFR2	mouse TNFR2
OPG	osteoprotegerin
OcN	osteoclast number
OcS	osteoclast surface
RSV	Rous Sarcoma virus
sRANKL	soluble RANKL
Tb.N	trabecular numbers
TRAP	tartrate-resistant acid phosphatase

References

1. Teitelbaum SL. Bone resorption by osteoclasts. Science. 2000; 289:1504–1508. [PubMed: 10968780]
2. Lacey DL, Timms E, Tan HL, Kelley MJ, Dunstan CR, Burgess T, Elliott R, Colombero A, Elliott G, Scully S, et al. Osteoprotegerin ligand is a cytokine that regulates osteoclast differentiation and activation. Cell. 1998; 93:165–176. [PubMed: 9568710]
3. Simonet WS, Lacey DL, Dunstan CR, Kelley M, Chang MS, Lüthy R, Nguyen HQ, Wooden S, Bennett L, Boone T, et al. Osteoprotegerin: a novel secreted protein involved in the regulation of bone density. Cell. 1997; 89:309–319. [PubMed: 9108485]
4. Li J, Sarosi I, Yan X-Q, Morony S, Capparelli C, Tan H-L, McCabe S, Elliott R, Scully S, Van G, et al. RANK is the intrinsic hematopoietic cell surface receptor that controls osteoclastogenesis and regulation of bone mass and calcium metabolism. Proc Natl Acad Sci USA. 2000; 97:1566–1571. [PubMed: 10677500]
5. Kong YY, Feige U, Sarosi I, Bolon B, Tafuri A, Morony S, Capparelli C, Li J, Elliott R, McCabe S, et al. Activated T cells regulate bone loss and joint destruction in adjuvant arthritis through osteoprotegerin ligand. Nature. 1999; 402:304–309. [PubMed: 10580503]
6. Kobayashi K, Takahashi N, Jimi E, Udagawa N, Takami M, Kotake S, Nakagawa N, Kinosaki M, Yamaguchi K, Shima N, et al. Tumor necrosis factor alpha stimulates osteoclast differentiation by a mechanism independent of the ODF/RANKL-RANK interaction. J Exp Med. 2000; 191:275–286. [PubMed: 10637272]
7. Azuma Y, Kaji K, Katogi R, Takeshita S, Kudo A. Tumor necrosis factor-alpha induces differentiation of and bone resorption by osteoclasts. J Biol Chem. 2000; 275:4858–4864. [PubMed: 10671521]
8. Kotake S, Udagawa N, Takahashi N, Matsuzaki K, Itoh K, Ishiyama S, Saito S, Inoue K, Kamatani N, Gillespie MT, et al. IL-17 in synovial fluids from patients with rheumatoid arthritis is a potent stimulator of osteoclastogenesis. J Clin Invest. 1999; 103:1345–1352. [PubMed: 10225978]
9. Adamopoulos IE, Bowman EP. Immune regulation of bone loss by Th17 cells. Arthritis Res Ther. 2008; 10:225. [PubMed: 18983698]
10. Sato K, Suematsu A, Okamoto K, Yamaguchi A, Morishita Y, Kadono Y, Tanaka S, Kodama T, Akira S, Iwakura Y, et al. Th17 functions as an osteoclastogenic helper T cell subset that links T cell activation and bone destruction. J Exp Med. 2006; 203:2673–2682. [PubMed: 17088434]
11. Adamopoulos IE, Chao CC, Geissler R, Laface D, Blumenschein W, Iwakura Y, McClanahan T, Bowman EP. Interleukin-17A upregulates receptor activator of NF-kappaB on osteoclast precursors. Arthritis Res Ther. 2010; 12:R29. [PubMed: 20167120]
12. Yu JJ, Ruddy MJ, Wong GC, Sfintescu C, Baker PJ, Smith JB, Evans RT, Gaffen SL. An essential role for IL-17 in preventing pathogen-initiated bone destruction: recruitment of neutrophils to

inflamed bone requires IL-17 receptor-dependent signals. Blood. 2007; 109:3794–3802. [PubMed: 17202320]

13. Yu JJ, Ruddy MJ, Conti HR, Boonanantanasarn K, Gaffen SL. The interleukin-17 receptor plays a gender-dependent role in host protection against Porphyromonas gingivalis-induced periodontal bone loss. Infect Immun. 2008; 76:4206–4213. [PubMed: 18591228]
14. Goswami J, Hernández-Santos N, Zuniga LA, Gaffen SL. A bone-protective role for IL-17 receptor signaling in ovariectomy-induced bone loss. Eur J Immunol. 2009; 39:2831–2839. [PubMed: 19731364]
15. Murphy CA, Langrish CL, Chen Y, Blumenschein W, McClanahan T, Kastelein RA, Sedgwick JD, Cua DJ. Divergent pro- and anti-inflammatory roles for IL-23 and IL-12 in joint autoimmune inflammation. J Exp Med. 2003; 198:1951–1957. [PubMed: 14662908]
16. Langrish CL, Chen Y, Blumenschein WM, Mattson J, Basham B, Sedgwick JD, McClanahan T, Kastelein RA, Cua DJ. IL-23 drives a pathogenic T cell population that induces autoimmune inflammation. J Exp Med. 2005; 201:233–240. [PubMed: 15657292]
17. Yago T, Nanke Y, Kawamoto M, Furuya T, Kobashigawa T, Kamatani N, Kotake S. IL-23 induces human osteoclastogenesis via IL-17 in vitro, and anti-IL-23 antibody attenuates collagen-induced arthritis in rats. Arthritis Res Ther. 2007; 9:R96. [PubMed: 17888176]
18. Chen L, Wei XQ, Evans B, Jiang W, Aeschlimann D. IL-23 promotes osteoclast formation by up-regulation of receptor activator of NF-kappaB (RANK) expression in myeloid precursor cells. Eur J Immunol. 2008; 38:2845–2854. [PubMed: 18958885]
19. Quinn JM, Sims NA, Saleh H, Mirosa D, Thompson K, Bouralexis S, Walker EC, Martin TJ, Gillespie MT. IL-23 inhibits osteoclastogenesis indirectly through lymphocytes and is required for the maintenance of bone mass in mice. J Immunol. 2008; 181:5720–5729. [PubMed: 18832731]
20. Chao CC, Chen SJ, Adamopoulos IE, Judo M, Asio A, Ayanoglu G, Bowman EP. Structural, cellular, and molecular evaluation of bone erosion in experimental models of rheumatoid arthritis: assessment by μCT, histology, and serum biomarkers. Autoimmunity. 2010; 43:642–653. [PubMed: 20380588]
21. Cua DJ, Sherlock J, Chen Y, Murphy CA, Joyce B, Seymour B, Lucian L, To W, Kwan S, Churakova T, et al. Interleukin-23 rather than interleukin-12 is the critical cytokine for autoimmune inflammation of the brain. Nature. 2003; 421:744–748. [PubMed: 12610626]
22. Suda T, Liu D. Hydrodynamic gene delivery: its principles and applications. Mol Ther. 2007; 15:2063–2069. [PubMed: 17912237]
23. Chen ZY, He CY, Kay MA. Improved production and purification of minicircle DNA vector free of plasmid bacterial sequences and capable of persistent transgene expression in vivo. Hum Gene Ther. 2005; 16:126–131. [PubMed: 15703495]
24. Chao CC, Chen SJ, Adamopoulos IE, Davis N, Hong K, Vu A, Kwan S, Fayadat-Dilman L, Asio A, Bowman EP. Anti-IL-17A therapy protects against bone erosion in experimental models of rheumatoid arthritis. Autoimmunity. 2010; 44:243–252. [PubMed: 20925596]
25. Lane NE, Yao W, Balooch M, Nalla RK, Balooch G, Habelitz S, Kinney JH, Bonewald LF. Glucocorticoid-treated mice have localized changes in trabecular bone material properties and osteocyte lacunar size that are not observed in placebo-treated or estrogen-deficient mice. J Bone Miner Res. 2006; 21:466–476. [PubMed: 16491295]
26. Wiekowski MT, Leach MW, Evans EW, Sullivan L, Chen SC, Vassileva G, Bazan JF, Gorman DM, Kastelein RA, Narula S, Lira SA. Ubiquitous transgenic expression of the IL-23 subunit p19 induces multiorgan inflammation, runting, infertility, and premature death. J Immunol. 2001; 166:7563–7570. [PubMed: 11390512]
27. Keffer J, Probert L, Cazlaris H, Georgopoulos S, Kaslaris E, Kioussis D, Kollias G. Transgenic mice expressing human tumour necrosis factor: a predictive genetic model of arthritis. EMBO J. 1991; 10:4025–4031. [PubMed: 1721867]
28. Nair RP, Duffin KC, Helms C, Ding J, Stuart PE, Goldgar D, Gudjonsson JE, Li Y, Tejasvi T, Feng BJ, et al. Collaborative Association Study of Psoriasis. Genome-wide scan reveals association of psoriasis with IL-23 and NF-kappaB pathways. Nat Genet. 2009; 41:199–204. [PubMed: 19169254]

29. Buonocore S, Ahern PP, Uhlig HH, Ivanov II, Littman DR, Maloy KJ, Powrie F. Innate lymphoid cells drive interleukin-23-dependent innate intestinal pathology. Nature. 2010; 464:1371–1375. [PubMed: 20393462]

30. Chen ZY, He CY, Ehrhardt A, Kay MA. Minicircle DNA vectors devoid of bacterial DNA result in persistent and high-level transgene expression in vivo. Mol Ther. 2003; 8:495–500. [PubMed: 12946323]

31. McGeachy MJ, Bak-Jensen KS, Chen Y, Tato CM, Blumenschein W, McClanahan T, Cua DJ. TGF-beta and IL-6 drive the production of IL-17 and IL-10 by T cells and restrain T(H)-17 cell-mediated pathology. Nat Immunol. 2007; 8:1390–1397. [PubMed: 17994024]

32. Rivollier A, Mazzorana M, Tebib J, Piperno M, Aitsiselmi T, Rabourdin-Combe C, Jurdic P, Servet-Delprat C. Immature dendritic cell trans-differentiation into osteoclasts: a novel pathway sustained by the rheumatoid arthritis microenvironment. Blood. 2004; 104:4029–4037. [PubMed: 15308576]

33. Arai F, Miyamoto T, Ohneda O, Inada T, Sudo T, Brasel K, Miyata T, Anderson DM, Suda T. Commitment and differentiation of osteoclast precursor cells by the sequential expression of c-Fms and receptor activator of nuclear factor kappaB (RANK) receptors. J Exp Med. 1999; 190:1741–1754. [PubMed: 10601350]

34. Jacquin C, Gran DE, Lee SK, Lorenzo JA, Aguila HL. Identification of multiple osteoclast precursor populations in murine bone marrow. J Bone Miner Res. 2006; 21:67–77. [PubMed: 16355275]

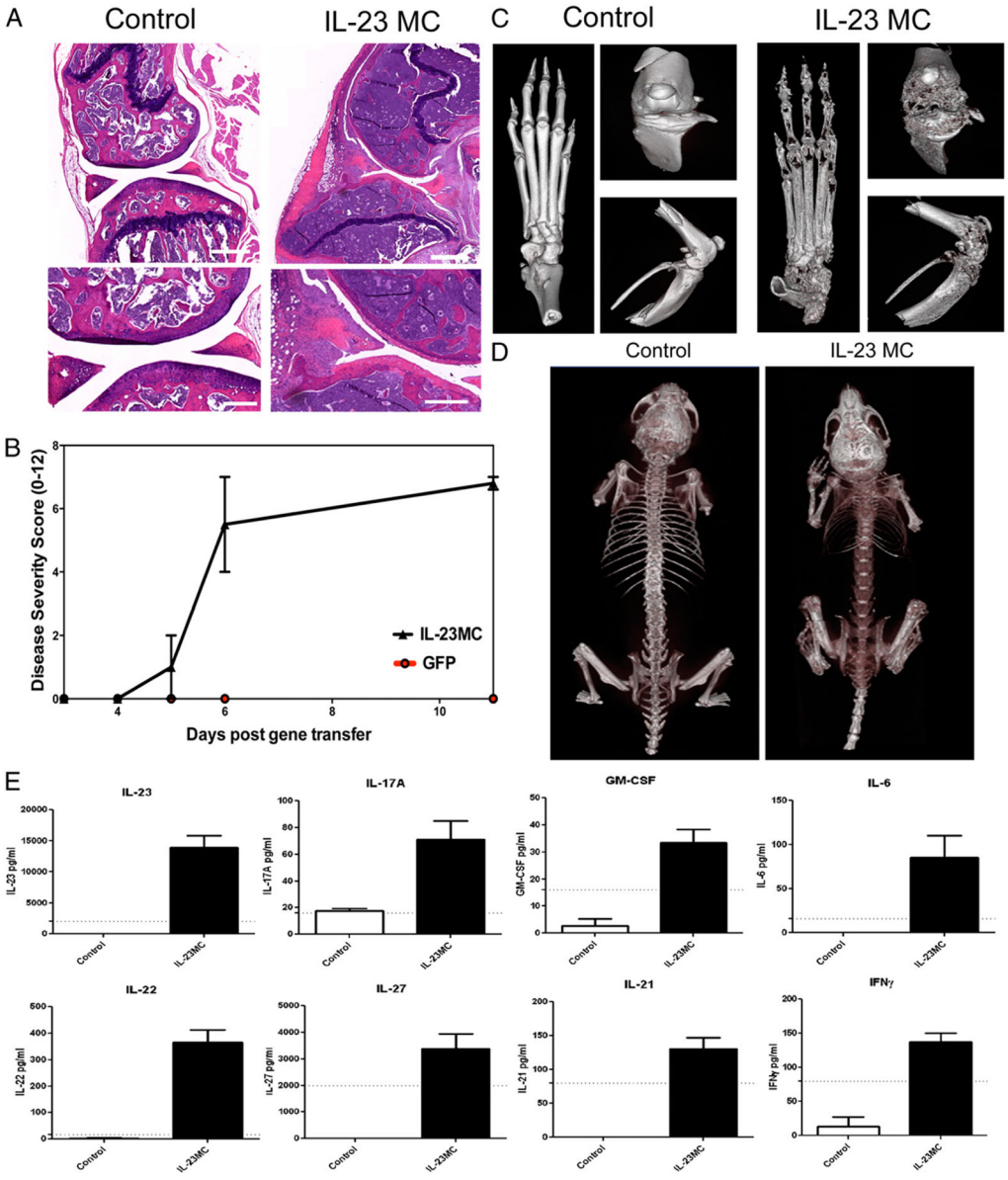

FIGURE 1.

Systemic IL-23 induces joint inflammation and extensive bone loss in vivo. *A*, H&E-stained decalcified sections of the knee joint showing extensive subchondral, metaphyseal, and epiphyseal bone loss, hyperplastic bone marrow, and pannus formation 30 d after IL-23 MC injection compared with GFP MC control. Scale bars, 500 μm (*top panels*) and 250 μm (*bottom panels*). Representative images of three independent experiments. *B*, Clinical disease severity score after IL-23 MC injection (average of four independent experiments). *C*, Three-dimensional rendered images from the paw and the anterior and side knee views 60 d after IL-23 MC injection (representative images from three independent experiments). *D*, Day 90 whole-body scan of control mice compared with the IL-23 MC-injected mice showing severe loss of bone mineral density in IL-23 MC-injected mice. *E*, Serum cytokine levels 28 d after IL-23 MC injection compared with GFP MC control mice. Cytokines presented were statistically different from control using serum data pooled from three

independent experiments. Dotted line shows sensitivity of the assay. $p < 0.05$, Mann–Whitney nonparametric test.

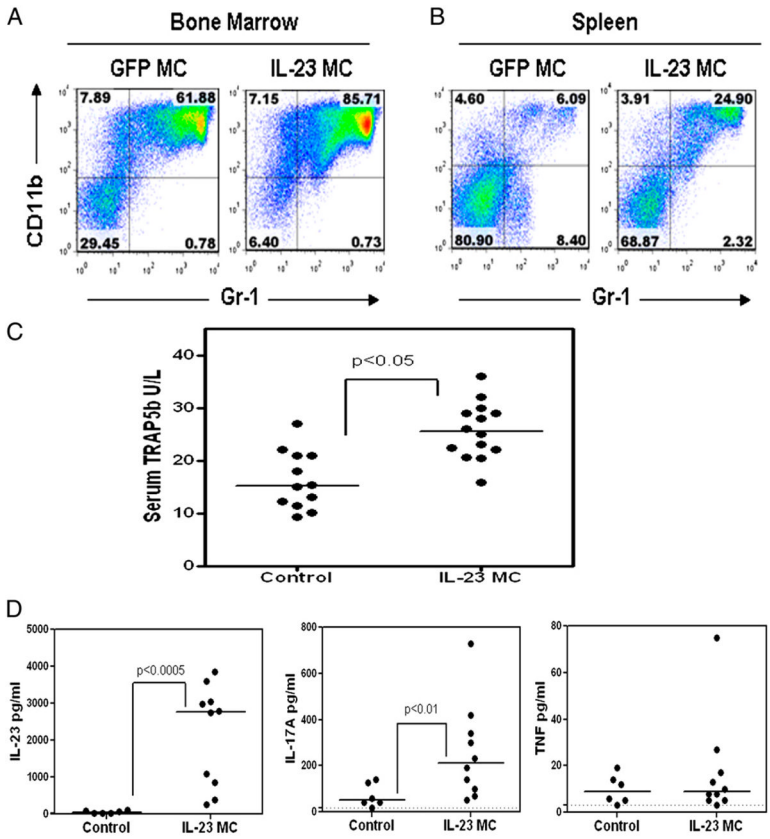

FIGURE 2.

Systemic IL-23 induces myelopoiesis, serum TRAP5b, and IL-17A. Flow cytometry of (*A*) bone marrow and (*B*) spleen 11 d after IL-23 MC injection compared with control GFP MC mice. *C*, Serum TRAP5b 11 d after IL-23 MC injection compared with GFP MC control ($p < 0.05$, Mann–Whitney nonparametric test; data pooled from four experiments). *D*, Serum IL-23, IL-17A, and TNF levels 11 d after IL-23 MC injection compared with GFP MC control ($p < 0.05$, Mann–Whitney nonparametric test; data pooled from three experiments).

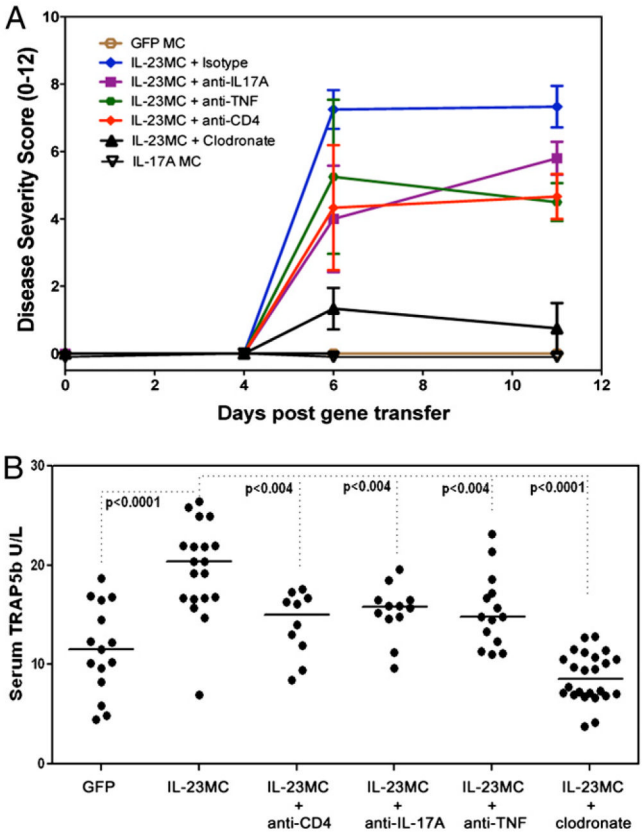

FIGURE 3.

Systemic IL-23–induced arthritis and elevated serum TRAP5b is inhibited by depletion of phagocytic cells. *A*, IL-23 MC induced arthritis after depletion of CD4 T cells or phagocytic cells, and neutralization of IL-17A or TNF. GFP MC and IL-17A MC controls also are presented (data pooled from three experiments). *B*, Serum TRAP5b 11 d after IL-23 MC injection (ANOVA).

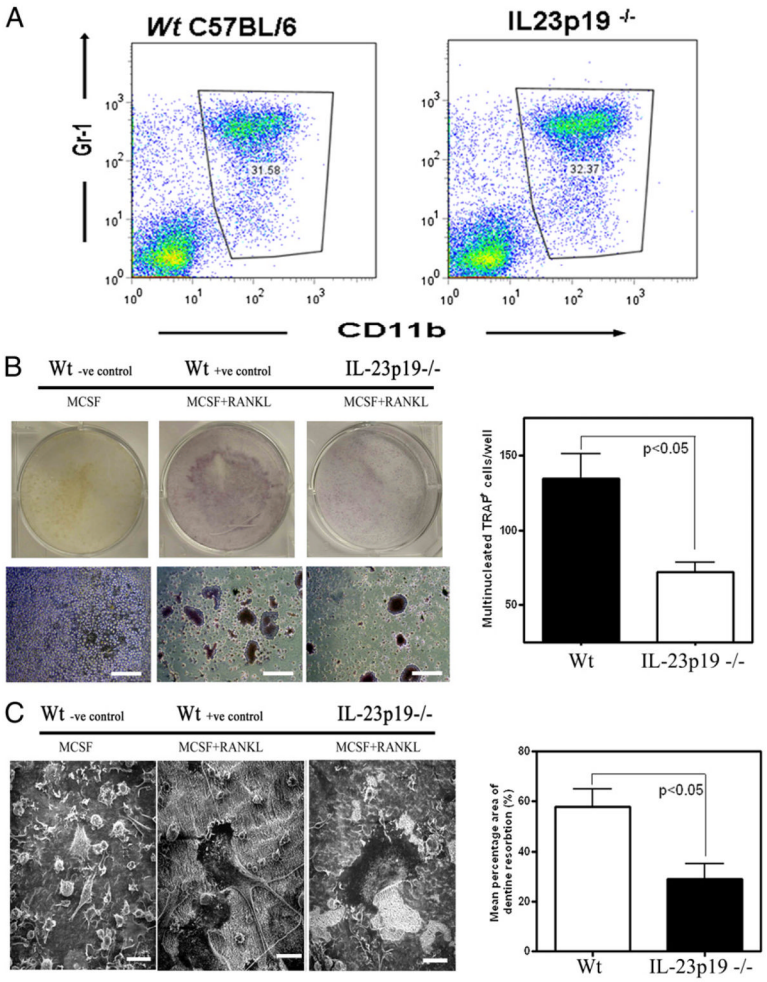

FIGURE 4.

IL-23p19$^{-/-}$ osteoclasts have impaired differentiation and function. *A*, Flow cytometry of bone marrow isolated from IL-23p19$^{-/-}$ or control mice cultured for 24 h in the presence of M-CSF. *B*, BMM isolated from IL-23p19$^{-/-}$ and control mice cultured for 6 d in the presence of M-CSF+RANKL form TRAP^{+} cells, which are also multinucleated (TRAP stain). Scale bars, 200 μm. *C*, Scanning electron photomicrographs of BMM cultures showing mature osteoclast resorbing activity (i.e., resorbed dentine has a rough, lighter color appearance). Scale bars, 50 μm. Representative data of three experiments done in triplicate.

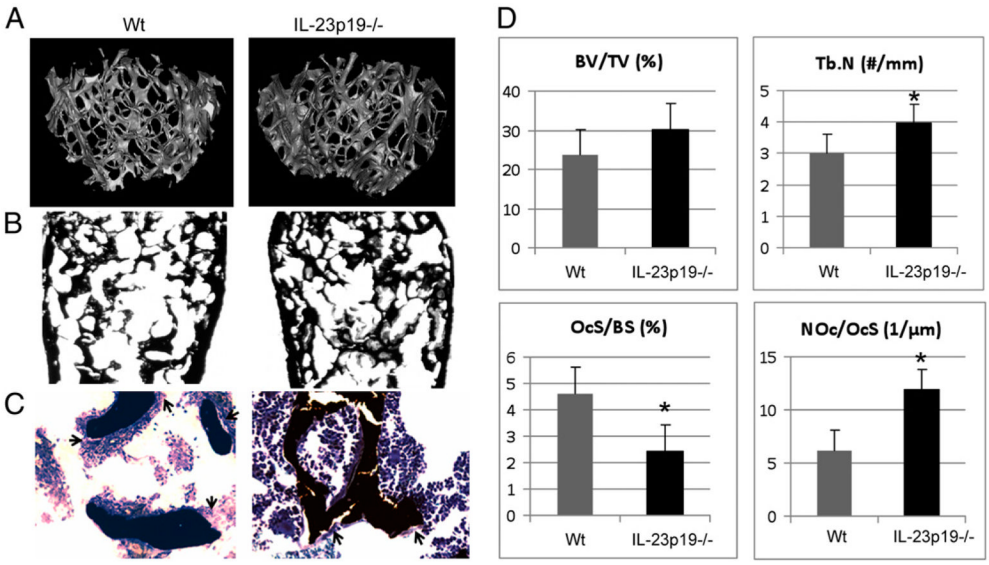

FIGURE 5.

Twenty-six–wk-old male IL-23–deficient mice have bone abnormalities caused by osteoclast dysregulation. *A*, Representative high-resolution μCT analysis of 26-wk-old male mouse's trabecular bone in the distal femur. *B*, Von Kossa-stained sections of 26-wk-old male mouse's distal femurs. Original magnification ×2. *C*, Toluidine blue counterstained von Kossa-stained sections of 26-wk-old male mouse's distal femurs. Original magnification ×20. Black arrows indicate osteoclasts. *D*, BV/TV, Tb.N, OcS/BS, and OcN/OcS (NOc/OcS) measured in the distal femur. **p* < 0.05.